

AERODYNAMIC AND STABILITY-DRIVEN PRE-DESIGN OF A FUEL-CELL POWERED FLYING WING AIRCRAFT

Philip Kirschnek[1], Samuel Lesak[1] & Andreas Tramposch[1]

[1]FH JOANNEUM GesmbH - University of Applied Sciences, Institute of Aviation, 8020 Graz, Austria

Abstract

Flying-wing configurations offer the potential for substantial aerodynamic efficiency gains over conventional tube-and-wing aircraft, but their practical realization is constrained by stringent aerodynamic and stability requirements. This paper presents a systematic longitudinal aerodynamic pre-design methodology for a fuel-cell-powered flying wing, intended for certification within the CS-23 category, constituting the first step of a broader multi-fidelity design workflow.

The aerodynamic analysis is performed with the panel method in OpenVSP, automated through a MATLAB-controlled parametric workflow, after establishing grid convergence by Richardson extrapolation. The wing twist distribution is varied to approximate Prandtl's bell-shaped spanload for improved flight behavior during roll-turns, and for each candidate geometry a coupled study of the center-of-gravity position, angle-of-attack and elevon deflection identifies the feasible trim points during unaccelerated horizontal flight. A static and dynamic longitudinal stability analysis is subsequently conducted for all trimmed configurations, assessing the aircraft's flight-dynamics by evaluating the static margin, the short-period and phugoid modes and the inherent recovery of the aircraft following a disturbance.

The wing twist is shown to be a primary design driver. Relative to the untwisted baseline, it expands the admissible center-of-gravity travel from $0.1\,\mathrm{m}$ to $0.4\,\mathrm{m}$ while only marginally reducing aerodynamic efficiency. The modal trends across the center-of-gravity range are quantified, the phugoid remaining stable throughout in accordance with the CS-23 requirements, and a comparison with RANS CFD confirms the applicability of the panel method within the stability-relevant angle-of-attack range. The methodology provides a structured and computationally efficient basis for the subsequent integration of higher-fidelity CFD, lateral-directional stability and fuel-cell thermal management.

Keywords: flying wing, fuel-cell, CS-23, longitudinal stability, flight dynamics

1. Introduction

Flying wings, which integrate the fuselage into the lifting airfoil, are regarded as aerodynamically highly efficient in contrast to conventional tube-and-wing aircraft (cf. [1]), being able to significantly reduce fuel-consumption and resulting greenhouse-gas emissions [2, 3, 4]. The elimination of the empennage reduces parasitic and interference drag and increases the effective lifting surface by lowering the wetted-to-wing-area ratio (cf. [5]). These aerodynamic advantages, however, must be balanced against the inherent stability and flight-dynamic disadvantages of tailless configurations. In conventional aircraft, longitudinal and directional stability are provided by the horizontal and vertical stabilizers, respectively. In tailless designs, both functions must be realized by the main lifting surface alone through a combination of airfoil shape, wing sweep, dihedral, and spanwise twist distribution. The location of the center-of-gravity (CG) relative to the neutral point (NP) critically determines the static margin and the resulting handling characteristics, making the coupled assessment of geometric, aerodynamic, and CG-related parameters essential already in the preliminary design phase.

A target lift distribution particularly suited to tailless aircraft is the bell-shaped spanload proposed by Prandtl [6], which redistributes the spanwise loading inboard and, through the resulting upwash

https://doi.org/10.71945/icas2026_0318

at the wingtip, produces proverse yaw behavior during rolling maneuvers [7]. Beyond these lateral-directional benefits, the associated washout twist directly affects the longitudinal characteristics by shifting the center-of-pressure and modifying the pitching moment. Although the aerodynamic potential of flying-wing and blended-wing-body configurations and their stability characteristics have been investigated extensively in isolation (cf. [8, 9]), structured preliminary design approaches that explicitly couple wing twist, CG location, trim, and longitudinal stability remain limited, particularly for small piloted aircraft in the CS-23 category.

Against this background, the present paper addresses the longitudinal aerodynamic pre-design of a fuel-cell-powered flying-wing aircraft intended for CS-23 certification. The wing twist distribution is varied parametrically to approximate Prandtl's bell-shaped spanload, and for each candidate geometry, a comprehensive CG, angle-of-attack, and elevon-deflection study is conducted to identify feasible trim points. A longitudinal stability analysis is subsequently performed for all trimmed configurations satisfying the defined stability criteria, characterizing the admissible CG travel, required elevon deflection, and dynamic modal behavior in unaccelerated horizontal flight. The methodology constitutes the first step of a broader multi-fidelity design workflow. Higher-fidelity CFD analyses, propulsion integration, lateral-directional stability, and fuel-cell thermal management are addressed in subsequent stages, as the fuel-cell architecture and associated mass distribution remain uncertain at this preliminary stage.

1.1 Flying Wing Baseline

A conceptual aircraft model is designed according to the CS-23 specifications and visualized in Figure 1. The outlined geometry is defined and used as the baseline throughout this work. The configuration follows a pure flying-wing layout without a separate horizontal or vertical tailplane.

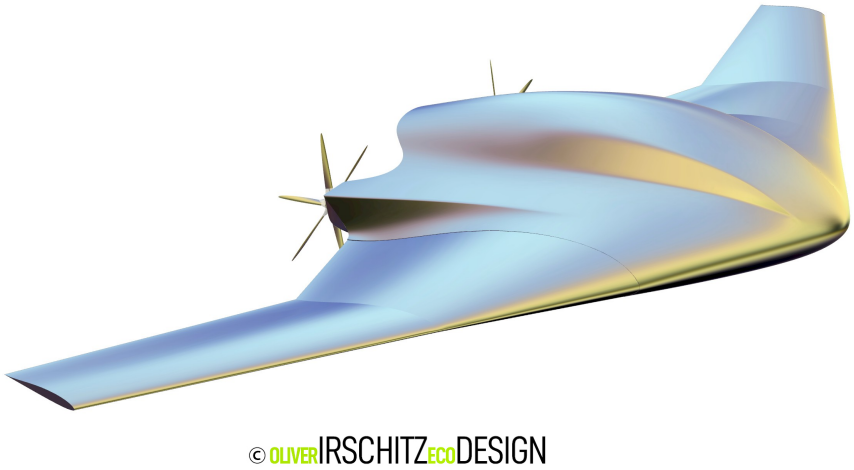


Figure 1 – Baseline design for the fuel-cell powered flying wing in the normal CS-23 category.

The key design parameters for the reference flying-wing subject to the aerodynamic/stability analysis are listed in Table 1. The values represent *initial* configuration parameters, and are expected to evolve throughout the preliminary design phase of the aircraft. The aircraft exhibits a moderate wing sweep angle of 30° without twist. The thick inboard airfoil profile accommodates the cabin volume required for passengers and pilots, while sections outboard of the cabin transition to a reflex profile with a modified thickness across different wing-sections. Performance-wise, the aircraft is expected to have a maximum take-off mass of $5000\,\mathrm{kg}$, cruising at $210\,\mathrm{kts}$ at an altitude of $16\,400\,\mathrm{ft}$. Propulsion is provided by a $400\,\mathrm{kW}$ hydrogen fuel-cell system with two pusher propellers, coupled with a battery providing instantaneous power output during increased demands.

1.2 Aerodynamic Design Considerations for Stable Aircraft Design

Since a tailless aircraft must realize flight stability through the main lifting surface alone, its spanwise lift distribution and airfoil shape become the central design parameters. The conventional elliptical

Table 1 – Key design parameters of the preliminary fuel-cell powered flying wing model.

Parameter	Symbol	Value
Geometry		
Airfoil Cabin	–	NACA 27025 – 44
Airfoil Root-Tip	–	MH62 – mod
Wingspan	b	19.9 m
Projected Wing area	S	77 m^2
Mean aerodynamic chord	$\bar{c}$	5.26 m
Root chord	c_r	9.30 m
Tip chord	c_t	1.10 m
Aspect ratio	AR	3.78
Taper ratio	λ	0.118
Leading-edge sweep	Λ_{LE}	30°
Dihedral angle	Γ	0°
Masses		
Maximum take-off mass	$MTOM$	5000 kg
Performance		
Cruise speed	V_C	210 kts
Cruise altitude	h_C	16400 ft
Maximum range	R_{max}	1080 NM
Propulsion		
Fuel cell power output	P_{FC}	400 kW
Number of propellers	n_P	2
Propeller configuration	–	Pusher
Certification		
Category	–	CS-23
Number of occupants	–	8+2

lift distribution, formulated by Prandtl [10] in 1923, minimizes the induced drag for a fixed wingspan and is therefore favored for tube-and-wing aircraft [11]. During roll, however, it generates an adverse yawing moment, where the downward-deflected aileron increases local lift and induced drag, yawing the aircraft opposite to the intended turn. In conventional aircraft, this movement is counteracted with the rudder. As tailless aircraft are designed without a distinct vertical tail, different philosophies are required to yaw the aircraft during roll.

A later formulation by Prandtl [6] in 1933 minimizes the induced drag under the constraint of a fixed root bending moment, yielding a wing that is $11\,\%$ more efficient with a $22\,\%$ larger span than a wing under elliptical loading and equal lift, yielding the bell-shaped spanload. The bell lift-distribution is formulated by Equation (1) [7] for the normalized lift distribution Γ as a function of the relative span location x.

$$\Gamma(x) = \left(1 - x^2\right)^{\frac{3}{2}} \tag{1}$$

The bell-shaped distribution redistributes the loading inboard through a washout twist, with a positive incidence angle at the root reducing to possibly negative twist at the tip. The reduced tip loading lowers the local downwash and may even induce a slight upwash, generating an induced-thrust component [7]. This induced thrust increases on the downward-moving aileron during roll, producing proverse yaw, making auxiliary yaw control during roll-turns unnecessary. A comparison of the elliptical and bell-shaped lift distributions across the half-wing is shown in Figure 2.

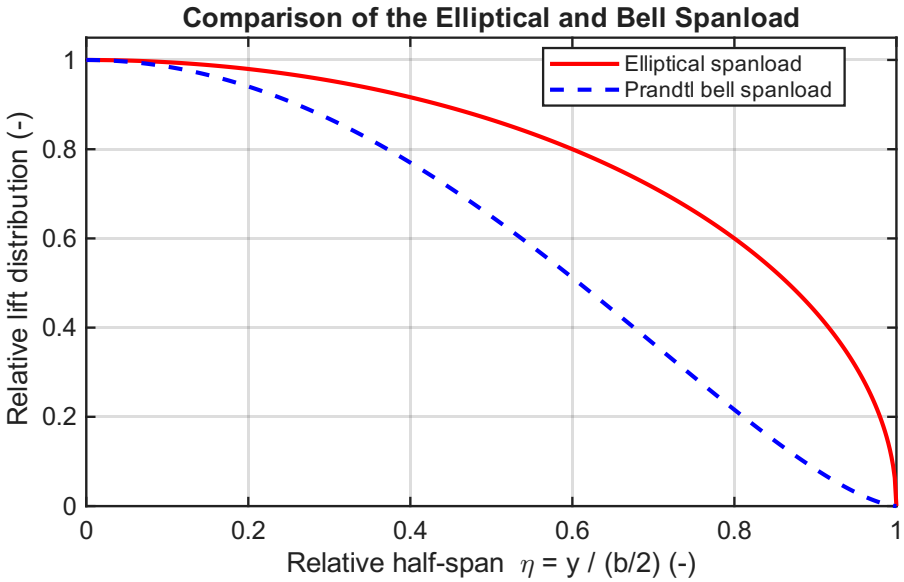


Figure 2 – Elliptical lift-load distribution vs. Prandtl's bell-spanload on the half-wing.

1.3 Static Longitudinal Stability

Static longitudinal stability of an aircraft is defined as the tendency of the aircraft to return to its equilibrium pitch attitude after being disturbed in the pitch axis, which is a flight-safety prerequisite for commercial aircraft. Ensuring and demonstrating static longitudinal stability is a certification requirement under the CS-23 standards, indicating that "The aeroplane must be longitudinally, directionally and laterally stable under CS 23.173 to 23.181" [12].

A viable steady flight state requires two distinct conditions to be satisfied about the center-of-gravity. The *trim condition* requires that the total pitching moment vanishes at the operating condition in terms of flight state, where $c_m|_{CG} = 0$. The *static stability condition* requires that a disturbance from this equilibrium produces a restoring moment, expressed through the pitching-moment coefficient gradient about the center-of-gravity being negative,

$$c_{m_\alpha} = \frac{\partial c_m}{\partial \alpha} < 0, \tag{2}$$

where c_m and α denote the pitching moment coefficient and the angle-of-attack, respectively [13, 14]. Thus, the trim condition sets *where* the equilibrium is located, whereas the stability condition determines whether the aircraft *returns* to it after a disturbance.

The pitching moment about the center-of-gravity is generated by the resultant aerodynamic force acting at the center-of-pressure. Its magnitude and sign depend on the position of the center-of-pressure relative to the center-of-gravity, and its variation with angle-of-attack determines the pitching moment gradient. The location of the center-of-pressure itself is governed by the airfoil shape through the pitching moment about the aerodynamic center $c_{m,ac}$, which is the location at the airfoil where the pitching moment remains constant across different angles-of-attack. Conventional cambered airfoils exhibit a negative $c_{m,ac}$, reflex airfoils with an upward-deflected trailing edge a small positive $c_{m,ac}$, and symmetric airfoils $c_{m,ac} = 0$ [15].

As the angle-of-attack – and thus the lift coefficient – increases, the center-of-pressure of a cambered airfoil moves forward toward the aerodynamic center, whereas that of a reflex airfoil moves rearward, and that of a symmetric airfoil remains fixed at the aerodynamic center [16]. This movement changes the moment arm between the resultant force and the center-of-gravity, and therefore the pitching moment M_y about the center-of-gravity, as illustrated in Figure 3. For a cambered airfoil, the forward-moving center-of-pressure produces a moment that becomes increasingly nose-up with

angle-of-attack, corresponding to a positive gradient; for a reflex airfoil, the rearward-moving center-of-pressure produces an increasingly nose-down moment and thus a negative, stabilizing gradient; for a symmetric airfoil, the fixed center-of-pressure yields a constant moment.

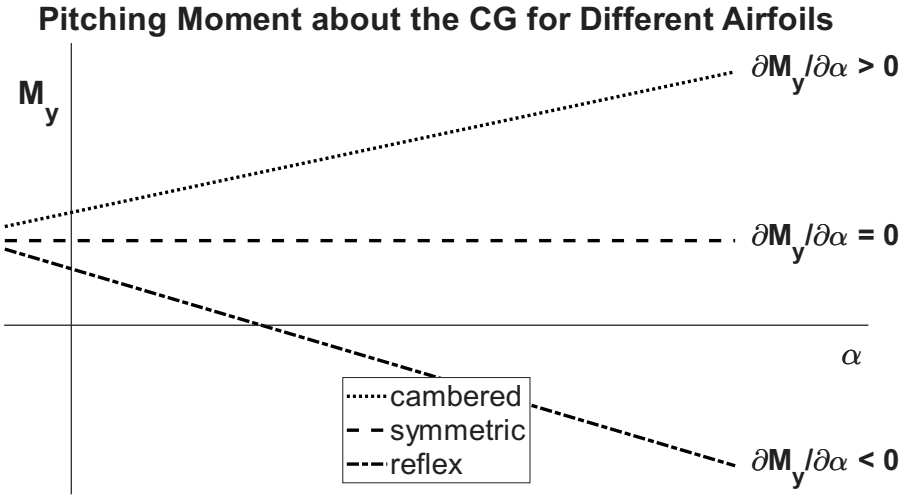


Figure 3 – Pitching moment about the center-of-gravity as a function of the angle-of-attack for the three airfoil types, resulting from the center-of-pressure movement associated with each airfoil.

It should be emphasized that this center-of-pressure description assumes a fixed reference point and illustrates the trim behavior; the sign of the gradient additionally depends on where the center-of-gravity is placed relative to the NP, which is the aerodynamic center for the entire aircraft. The stability condition is expressed most generally in terms of both the neutral point x_{NP} and the center-of-gravity position x_{CG} [13],

$$c_{m_\alpha} = -c_{L_\alpha}\left(\frac{x_{NP} - x_{CG}}{\bar{c}}\right) = -c_{L_\alpha} \cdot SM, \tag{3}$$

with the mean aerodynamic chord $\bar{c}$, the lift-curve slope c_{L_α} and the static margin SM. Under the assumption $c_{L_\alpha} > 0$, a positive static margin – the NP aft of the center-of-gravity – yields the required $c_{m_\alpha} < 0$, independent of the airfoil shape. The airfoil hence governs the trim condition through its $c_{m,ac}$, while static stability is set by the center-of-gravity position relative to the neutral point. Thus, reflex airfoils are particularly suited to tailless configurations, as their positive $c_{m,ac}$ allows the aircraft to be trimmed at a positive lift coefficient while the center-of-gravity remains ahead of the neutral point, upon first assessment satisfying the trim and static stability requirements (cf. [17]). Further, increased angles-of-attack should yield a restoring pitching moment around the CG back to trim conditions due to the rearward movement of the center-of-pressure.

1.4 Dynamic Longitudinal Stability

Dynamic longitudinal stability is defined by its two oscillatory modes; the short-period oscillation and the long-period (phugoid). A short-period oscillation is a heavily damped pitch oscillation where the angle-of-attack changes at a constant airspeed. The long-period involves slow but significant changes in altitude and airspeed. Thus, the dynamic stability concerns the time-response after a perturbation [14]. The frequency of the eigenmode and its damping must satisfy regulatory handling-qualities, with the short-period only defined in the CS-23 as “Any short period oscillation [...] must be heavily damped [...]” [12]. Similarly, the phugoid is noted as “Any long-period oscillation of the flight path (phugoid) must not be so unstable as to cause an unacceptable increase in pilot workload or otherwise endanger the aeroplane” [12]. Hence, the requirements are of a qualitative nature; however, they shall still be ensured.

Both stability modes depend on a combination of aerodynamic derivatives and the mass/inertia of the aircraft. Aerodynamic derivatives can be estimated from various numerical models, including time-spectral stability derivative formulations [18], reduced frequency methods [19], and others (cf. [20, 21]). In this work, the simulation framework OpenVSP and its underlying panel solver

are employed to evaluate aerodynamic derivatives, whereas detailed information on mass distribution and inertia moments is usually defined in a more detailed design phase. For this study, estimated target values representing aircraft mass are employed.

2. Methods

This section discusses the methods used for analyzing the aerodynamic behavior of the flying wing. The aerodynamic analysis at the preliminary design stage is performed using the three-dimensional panel method, that relies on the assumption of inviscid, incompressible, and irrotational flow, governed by Laplace's equation for the velocity potential [16, 22]. With the results of the aerodynamic analysis outlining aerodynamic coefficients and its derivatives, a subsequent static and dynamic stability analysis can be performed. Within this work, MATLAB R2025b [23] is used to conduct the longitudinal stability analysis in the first phase. The workflow is outlined and described.

2.1 Mathematical Foundation of the Panel-Method

The aerodynamic analysis is carried out using VSPAERO and its panel solver within OpenVSP [24], whose implementation follows the low-order constant source-doublet panel formulation introduced by Maskew [25]. Panel methods solve potential flows around two- and three-dimensional bodies by replacing the geometry with source and doublet panels that satisfy the boundary conditions on the body and across the wake [26]. The underlying governing equation is the Prandtl-Glauert equation, derived from the Navier-Stokes equations under the assumptions of adiabatic, inviscid, irrotational, and linearized flow [22]:

$$\left(1 - Ma_\infty^2\right) \frac{\partial^2 \phi}{\partial x^2} + \frac{\partial^2 \phi}{\partial y^2} + \frac{\partial^2 \phi}{\partial z^2} = 0, \tag{4}$$

with the perturbation velocity potential ϕ and freestream Mach number Ma_∞. The point source and the point doublet are fundamental analytical solutions of Equation (4). Owing to the linearity of the equation, the total potential at an arbitrary field point is constructed by superimposing the freestream potential ϕ_∞ with the perturbation contributions ϕ_S and ϕ_D from the surface source and doublet distributions, which model thickness and circulation, respectively [27]:

$$\phi = \phi_\infty + \phi_S + \phi_D. \tag{5}$$

For the discrete formulation, the aircraft surface is divided into a network of quadrilateral panels, each carrying a constant-strength source and doublet distribution and one control point at the panel centroid [25, 27]. The unknown singularity strengths are determined such that the flow-tangency condition on the body and the Kutta condition along the trailing edges are simultaneously satisfied. The perturbation potential is prescribed to be zero on the interior side of each panel, representing a wall, while its source strength σ is fixed by the local freestream component normal to the surface [25, 28]:

$$\phi_{\text{int}} = 0, \qquad \sigma = -\vec{V}_\infty \cdot \hat{n}, \tag{6}$$

with $\hat{n}$ denoted as the outward surface normal and the freestream velocity vector $\vec{V}_\infty$. By integrating the source strength across the panel, the source potential is obtained. This formulation reduces the unknowns to the doublet strengths alone, yielding a smaller linear system [25, 27]. The Kutta condition is imposed implicitly by setting the wake-panel doublet strength equal to the difference of the adjacent upper and lower trailing-edge doublets [25]. Assembling the panel contributions yields a dense linear system for the doublet strengths as unknown singularity parameters $\{\lambda\}$ in Equation (7) [26, 27]:

$$[\text{AIC}]\{\lambda\} = \{b\}, \tag{7}$$

where each entry of the aerodynamic influence coefficient matrix $[\text{AIC}]$ quantifies how strongly the singularity of one panel affects the boundary condition at the control point of another. The right-hand side $\{b\}$ contains the freestream contributions imposed at each control point, and the solution of the system provides the doublet strengths on all panels. Subsequently, surface velocities are obtained

from a local spline fit of the resulting potential of Equation (5) [25], from which the local pressure coefficient is evaluated as [26]

$$c_p = 1 - \frac{U_t^2}{U_\infty^2}, \tag{8}$$

with U_t the local tangential velocity at the panel surface and U_∞ the freestream velocity magnitude. Integration of the pressure distribution over the body surface yields the aerodynamic forces and moments, with the induced drag being evaluated separately by a Trefftz-plane in the far-field.

2.2 Mathematical Foundation of the Longitudinal Stability Analysis

The mathematical model for the longitudinal stability analysis is linearized around the trim point for small perturbations. The aircraft is assumed to be a rigid body with a plane of symmetry, such that the longitudinal and lateral-directional dynamics can be described by first-order linear state space equations [29]. The present analysis is restricted to the longitudinal dynamics evaluated at the trimmed configurations identified in the workflow described in the upcoming section.

The longitudinal motion is described in body-fixed stability axes by the state vector $\vec{x}_{\text{lon}}$

$$\vec{x}_{\text{lon}} = \begin{bmatrix} u & \alpha & q & \theta \end{bmatrix}^T, \tag{9}$$

with the perturbations of the forward velocity u, the angle-of-attack, the pitch rate q and the pitch attitude θ [13, 29]. Instead of the angle-of-attack, the vertical velocity component w is often written, which relates to α through the small-perturbation approximation $\alpha \approx w/V_0$, where V_0 denotes the trim airspeed [13].

Linearization of the longitudinal force and moment equations around the trim condition, assuming straight and level flight ($\gamma_0 = 0$, $\theta_0 = \alpha_0$) and exploiting the aircraft's symmetry, yields the linear time-invariant state-space representation in Equation (10):

$$\dot{\vec{x}}_{\text{lon}} = A_{\text{lon}}\vec{x}_{\text{lon}} + B_{\text{lon}}\vec{u}_{\text{lon}}, \tag{10}$$

where $\vec{u}_{\text{lon}}$ contains the longitudinal control inputs, in the present case the elevon and flap deflection δ_e and δ_f, respectively [29]. The system matrix A_{lon} is assembled from the dimensional aerodynamic stability derivatives as

$$A_{\text{lon}} = \begin{bmatrix} X_u & X_\alpha & 0 & -g\cos\theta_0 \\ \dfrac{Z_u}{V_0} & \dfrac{Z_\alpha}{V_0} & 1+\dfrac{Z_q}{V_0} & -\dfrac{g\sin\theta_0}{V_0} \\ M_u & M_\alpha & M_q & 0 \\ 0 & 0 & 1 & 0 \end{bmatrix}, \tag{11}$$

with the gravitational acceleration g and the trim airspeed V_0 [29]. The entries X, Z and M denote the dimensional longitudinal stability derivatives of the body-axis forces along the x- and z-direction and of the pitching moment, respectively, normalized by the aircraft mass m for the force terms and by the pitch moment of inertia I_{yy} for the moment terms [29]. The subscripts indicate the perturbation state with respect to which each derivative is taken. The dimensional derivatives are obtained from the non-dimensional aerodynamic derivatives computed by VSPAERO using the reference area, the mean aerodynamic chord and the trim dynamic pressure [13, 29].

The input matrix B_{lon} is constructed analogously from the elevon and flap control derivatives [29] extracted from the VSPAERO stability output.

$$B_{\text{lon}} = \begin{bmatrix} X_{\delta_e} & X_{\delta_f} \\ \dfrac{Z_{\delta_e}}{V_0} & \dfrac{Z_{\delta_f}}{V_0} \\ M_{\delta_e} & M_{\delta_f} \\ 0 & 0 \end{bmatrix} \tag{12}$$

The previously described static longitudinal stability criterion $c_{m_\alpha} < 0$, already discussed above, represents the necessary but not sufficient condition for dynamic stability. Hence, the sufficient condition requires that all eigenvalues of A_{lon} have strictly negative real parts [13].

Eigenvalue analysis and modal identification. Solving the characteristic Equation (13) yields a pair of two longitudinal eigenvalues that, for a conventional aircraft, correspond to their short-period mode and the phugoid mode [13, 29].

$$\det\left(A_{\text{lon}} - \lambda I\right) = 0 \tag{13}$$

Each conjugate complex pair $\lambda_{1,2} = -\zeta\,\omega_n \pm \mathrm{j}\,\omega_d$ is characterized by an undamped natural frequency ω_n, and a damping ratio ζ, with the damped natural frequency $\omega_d = \omega_n\sqrt{1-\zeta^2}$.

Resulting from the eigenvalues, the short-period mode depicts a high eigenfrequency and pitch damping, resulting in quick angle-of-attack changes at a constant airspeed. The phugoid, in contrast, has a low frequency and damping ratio, resulting in a pitch attitude motion of the aircraft.

Root locus and dynamic response to perturbations. The eigenvalues of A_{lon} are plotted in the complex plane to visualize the migration of the longitudinal modes across the parameter sweep over CG position and wing twist. The root-locus representation is used to evaluate the impact of a variation in system parameters on a linear-time-invariant system in terms of stability. In addition, the time response of the longitudinal system to a perturbation in the forward velocity is computed by integrating Equation (10) for the trimmed configurations. This provides information on the dynamic behavior of the aircraft and its inertia.

2.3 Workflow

This work combines multiple software applications to analyze the aerodynamic behavior of the fuel-cell powered flying-wing. Thus, a predefined workflow must be established to properly assess the aircraft's dynamics in unaccelerated horizontal flight.

The designed aircraft is first simplified and modeled within OpenVSP, see Figure 4, with the aircraft's paneling, neglecting propellers and other external features. A subsequent grid refinement study provides insight into desirable grid spacing to minimize computational effort while maximizing the quality of results and determining the *discretization error*. The grid convergence study refers to Richardson's extrapolation method [30, 31], with the target parameter being the lift coefficient in the first place. The chosen grid discretization is employed for subsequent simulations to ensure comparability of results.

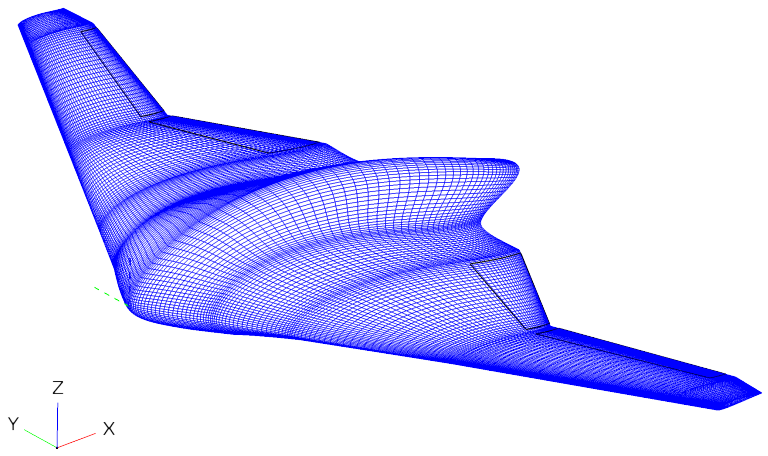


Figure 4 – Baseline aircraft geometry in OpenVSP with 3D-paneling and trailing edge control surfaces with inboard flaps and outboard elevons.

The baseline geometry's aerodynamic properties, without twist, dihedral, and directional control surfaces, are assessed to have a predefined starting point. The complete workflow for the stability estimation and its impact on the design is provided in the following paragraphs.

1. Twist study for the bell-shaped spanload For the baseline, the spanwise twist distribution is varied via a parameter study to approximate the bell-spanload [6, 7]. Geometries whose computed spanwise lift distribution show the closest agreement with Equation (1) are retained as candidate configurations for the subsequent steps.

2. Center-of-gravity, angle-of-attack and elevon-deflection study For each candidate geometry, a three-dimensional parameter study is conducted over the center-of-gravity position x_{CG}, the angle-of-attack, and the elevon deflection. For every (x_{CG}, α) combination, the elevon deflection is varied in a predefined range.

3. Trim-point evaluation The full simulation database is processed to extract, for each (x_{CG}, α) combination, the corresponding trim point at which $c_m = 0$ is achieved as a function of the elevon deflection. In the trim point, aircraft weight must be compensated by aircraft lift, whereas a positive lift-to-drag ratio is required. The resulting set of trim points defines the theoretically feasible design space.

4. Static longitudinal stability analysis at trimmed conditions A longitudinal stability analysis is performed for the trimmed candidate configurations in steady level flight, evaluating the relevant longitudinal stability derivatives at every trim point identified in Step 3. The stability output is subsequently filtered depending on the static margin and lift-generation in trim, reducing the large set of $c_m = 0$ points to a smaller subset of *true* trim points that satisfy the defined trim constraints.

5. Dynamic longitudinal stability evaluation of selected trim points. The reduced set of true trim points is analyzed individually with respect to their pitching moment coefficient and the associated static margin. The trim points are evaluated according to their time-dependent behavior, analyzing the system's response to changed initial conditions.

6. Geometry refinement based on stability derivatives. Based on the results of Step 5, the geometry is refined with the objective of improving the lateral-directional stability of the aircraft, while keeping longitudinal stability within the design range. The full workflow is iterated for further geometric design parameters, considering wing sweep and dihedral. The airfoil shape itself is not modified within the present study and is retained as a fixed input parameter.

3. Results

The results are split into three segments. The first outlines the grid convergence of the panel-solver. After agreeing on a grid size, the different twist configurations are evaluated, assessing the twist distribution that shows the best agreement with the bell-lift distribution. The most promising cases are subsequently analyzed in terms of their longitudinal stability. The VSPAERO simulation of the baseline geometry is compared to CFD to verify the applicability of the proposed method for the given analysis.

3.1 Richardson Extrapolation for Grid Convergence Evaluation

The Richardson extrapolation is used to quantify the uncertainty of the numerical results as a consequence of coarse grid spacing [32]. It allows to examine the discretization error of numerical methods. Theoretically, with an infinite grid refinement and reduction in time step size, the discretization error should approach zero [30].

Three grid sizes of the aircraft shown in Figure 4 were analyzed, using a coarse, medium, and fine spatial discretization. The coarse grid used 3500 elements distributed across the aircraft skin, with 4270 and 9709 panels defined for the medium and fine mesh, respectively.

The lift coefficient of the baseline aircraft at 0° angle-of-attack was defined as the relevant quantity of interest for the Richardson extrapolation and grid convergence index analysis. The influence of mesh refinement is illustrated in Figure 5.

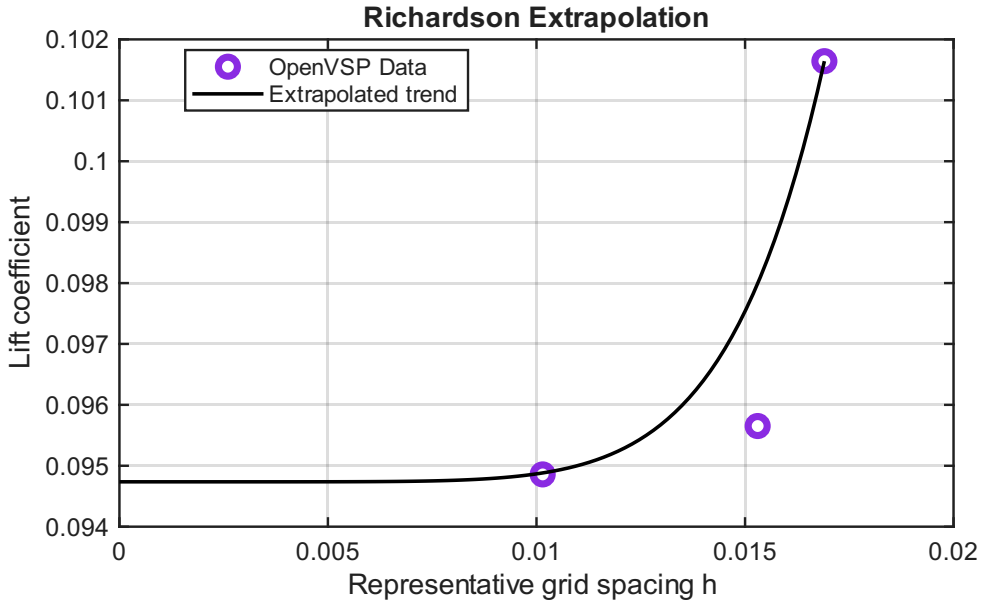


Figure 5 – Grid refinement study according to the Richardson extrapolation.

The effective grid refinement ratios were computed as $r_{21} = 1.508$ and $r_{32} = 1.105$, resulting in an effective ratio of $r_{\text{eff}} = 1.306$. The Richardson-extrapolated zero-grid-spacing value of the lift coefficient was $c_{\text{L,ext}} = 0.0947$. The fine-grid uncertainty was $GCI_{21} = 0.160\%$, while the medium-grid uncertainty was $GCI_{32} = 1.197\%$. The ratio $GCI_{32}/GCI_{21} = 7.478$ was in close agreement with the theoretical asymptotic ratio $r_{\text{eff}}^{p} = 7.541$, indicating that the fine solution is approximately within the asymptotic range of convergence. As the medium grid shows good agreement with the Richardson-extrapolated solution and provides a significantly reduced computational cost compared to the fine grid, it was selected for all subsequent simulations.

3.2 Airfoil Twist Variation

The airfoil twist is varied within a predefined range at each spanwise airfoil section. Under the assumption of a washout twist distribution, the root twist is constrained to be greater than the tip twist. A positive incidence angle is therefore specified at the inboard sections, while a negative twist is prescribed towards the wingtip. The maximum incidence at the centerline section is limited to 2°, with further inboard sections allowed up to 5° twist, whereas the outboard tip twist is limited to a minimum value of -12°. The local twist gradient between adjacent sections is additionally restricted to a maximum of $\pm 2\,^\circ\,\text{m}^{-1}$.

The spanwise lift distributions resulting from the parametric twist variation are normalized with respect to the local lift generated at the aircraft centerline and plotted as a function of the relative spanwise location in Figure 6. The agreement of each simulated distribution with Prandtl's theoretical bell-shaped spanload is quantified by the root-mean-square error between simulation and theory. The coefficient of determination R^2 is reported as a normalized measure of the explained variance. The three twist configurations with the lowest RMSE at an angle-of-attack of 0° are highlighted in Figure 6, alongside the configurations yielding the highest lift-to-drag ratio for reference.

The three configurations with the closest agreement to the theoretical curve exhibit similar twist distributions, with only minor variations in the tip region. Configurations yielding the highest lift-to-drag ratio at the same angle-of-attack approximate a more elliptical load distribution with reduced washout and higher mid-wing loading in comparison, consistent with theory [7, 10]. The resulting performance penalty of the bell-spanload configurations with respect to pure aerodynamic efficiency outlines a trade-off with benefits in lateral-directional dynamics.

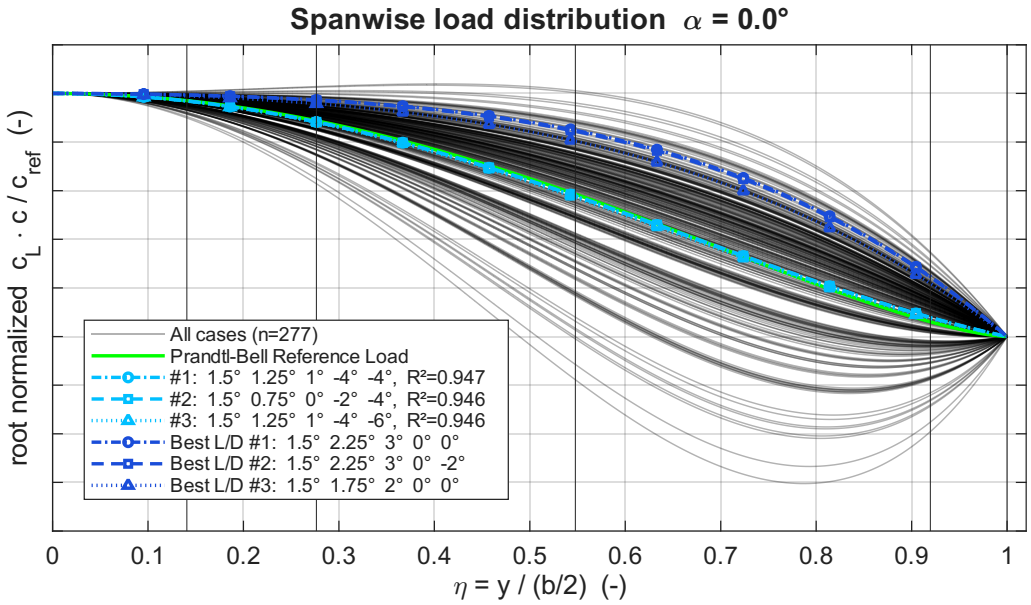


Figure 6 – Normalized spanwise lift distribution for the twist parameter variation at 0° angle-of-attack, with the three configurations closest to Prandtl's bell-shaped spanload and the highest-L/D reference case highlighted.

The subsequent stability analysis is performed for the untwisted baseline configuration and for the three twist configurations exhibiting the best agreement with the theoretical bell-shaped spanload to demonstrate achievable changes in aircraft dynamics by twisting the airfoil.

3.3 Dynamic Longitudinal Stability

The root-locus representation is used to assess the dynamic stability of the aircraft and the modal characteristics of its longitudinal motion. A configuration is dynamically stable if all eigenvalues of the longitudinal system matrix A_{lon} have strictly negative real parts, such that any perturbation decays over time. The dynamic stability analysis is restricted to statically stable trim points.

3.3.1 Longitudinal Eigenvalue Evaluation

The root-locus of all longitudinal eigenvalues for the baseline configuration and the three most promising twist variants outlined previously is shown in Figure 7, visualizing the short-period and phugoid as the longitudinal modes. As the lift-to-drag ratio increases towards the highest L/D trim configuration, the short-period damping ratio increases, while the undamped natural frequency decreases. This is a result of the counteracting behavior of the aircraft to perturbations in the pitch axis. The increase in L/D for each case is attributed to decreased control surface deflections to satisfy trim requirements, thereby reducing the trim drag as the center-of-gravity shifts rearward towards the neutral point. Consequently, a shift in the static margin of the aircraft results in a reduced (damped) natural frequency as the aircraft exhibits a lower gradient in pitching moment coefficient.

The phugoid's eigenvalues, shown in the right of Figure 7, lie close to the imaginary axis and are characterized by small damping ratios and very low natural frequencies, consistent with the slow exchange between kinetic and potential energy that governs the long-period mode, meeting the qualitative stability requirements in the CS-23, without considering controllability and handling properties.

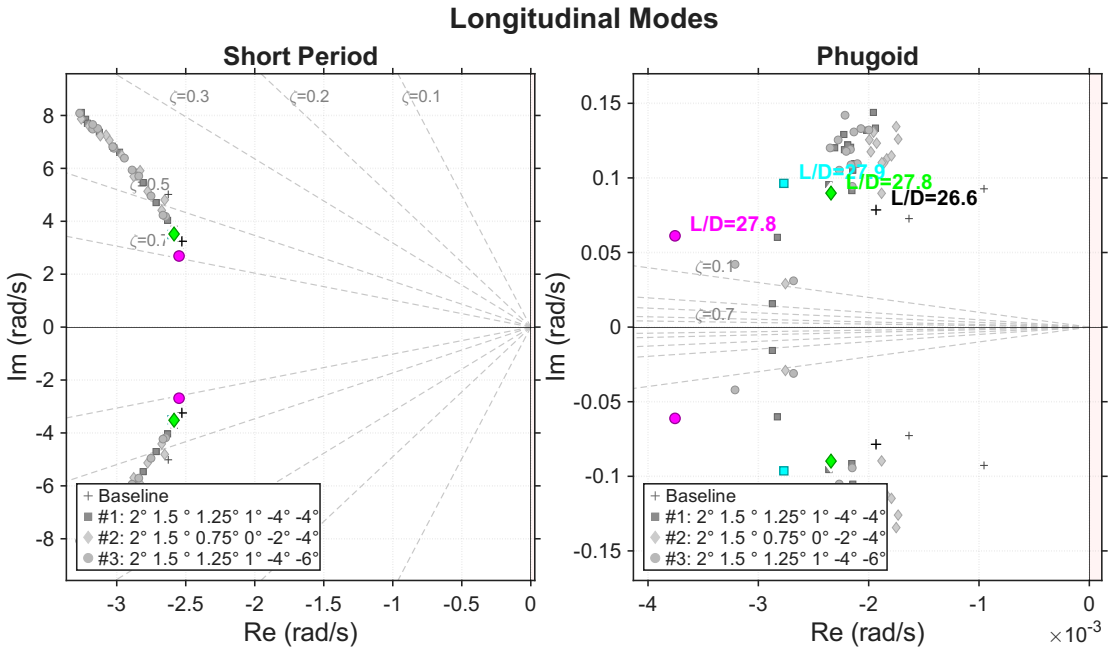


Figure 7 – Separation of the longitudinal modes into the short-period (left) and the phugoid (right) eigenvalues for the untwisted baseline and the three most promising bell-spanload twist configurations.

Beyond the modal characteristics, the twist variation has a strong effect on the feasible trim space and CG-travel. Only three *true* trim points satisfying the static stability criterion and the elevon authority limits were identified for the untwisted baseline, whereas approximately 15 feasible trim points were obtained for each of the twisted candidate geometries. This highlights the importance of wing twist as a primary design driver for tailless aircraft, not only contributing to proverse yaw but also increasing the CG travel range from $0.1\,\mathrm{m}$ with the baseline to $0.4\,\mathrm{m}$ with the twisted airfoils.

The effect on the lift-to-drag ratio is small but notable, with the best-case baseline reaching a glide ratio of 26.6, and the twist cases up to 27.9, as the inboard lift redistribution comes with a lift reduction outboard. The calculated values are slightly higher than values reported in literature [33, 34], which is attributed to the simulation method used herein and the omission of excrescence drag, propellers, ducting, and venting, or internal aerodynamics in general.

3.4 Free Response of the Phugoid and Short-Period

The temporal evolution of the longitudinal modes is analyzed to illustrate how the aircraft recovers from a disturbance under stick-fixed conditions. The free response reveals the resulting motion of the aircraft through its state variables.

An initial forward-velocity perturbation of $\Delta u_0 = 4\,\mathrm{m\,s^{-1}}$ is prescribed, with all remaining states initialized at their trim values. The free response of the linearized system, Equation (10), is integrated and separated into a short-period transient and a slow phugoid recovery.

The free response is compared to determine the best lift-to-drag ratio for each configuration's preferred twist and trim point in Figure 8, outlining the impact of varied wing twist.

Since the velocity perturbation acts on a state dominated by the phugoid, the short-period mode is only weakly excited, and the resulting angle-of-attack and pitch-rate transients decay within approximately one second, with the untwisted baseline initially showing the largest short-period excursion. The forward velocity and coupled pitch attitude are recovered slowly due to the lightly damped phugoid, whose oscillation decays slowly over several minutes, with case *3* depicting the lowest damped natural frequency and highest damping.

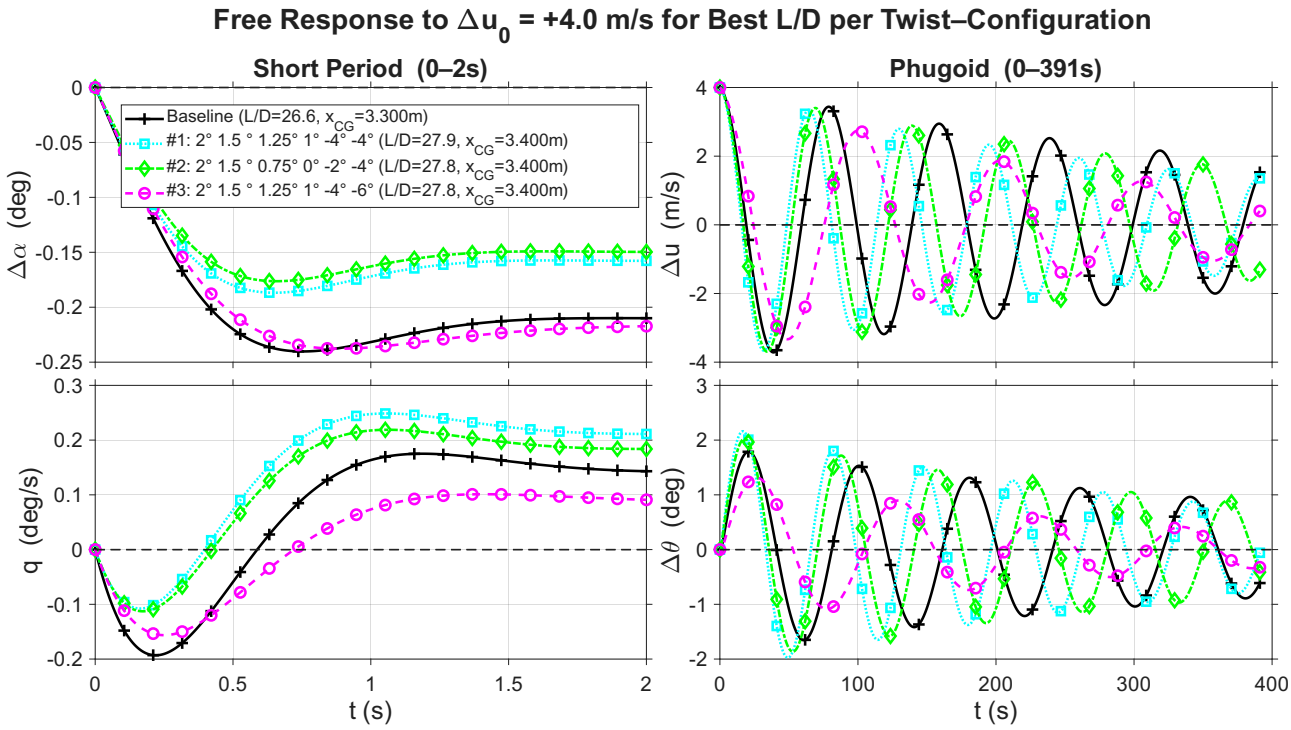


Figure 8 – Free response to an initial forward-velocity perturbation of $4\,\mathrm{m\,s^{-1}}$ for the baseline and twisted configurations at their best L/D showing the short-period (left) and phugoid (right) recovery.

To isolate the effect of the static margin from the wing geometry, the center-of-gravity position is varied for a single twist configuration. The influence of the center-of-gravity travel on the short-period and phugoid recovery is shown in Figure 9 for the twist-case number *1*.

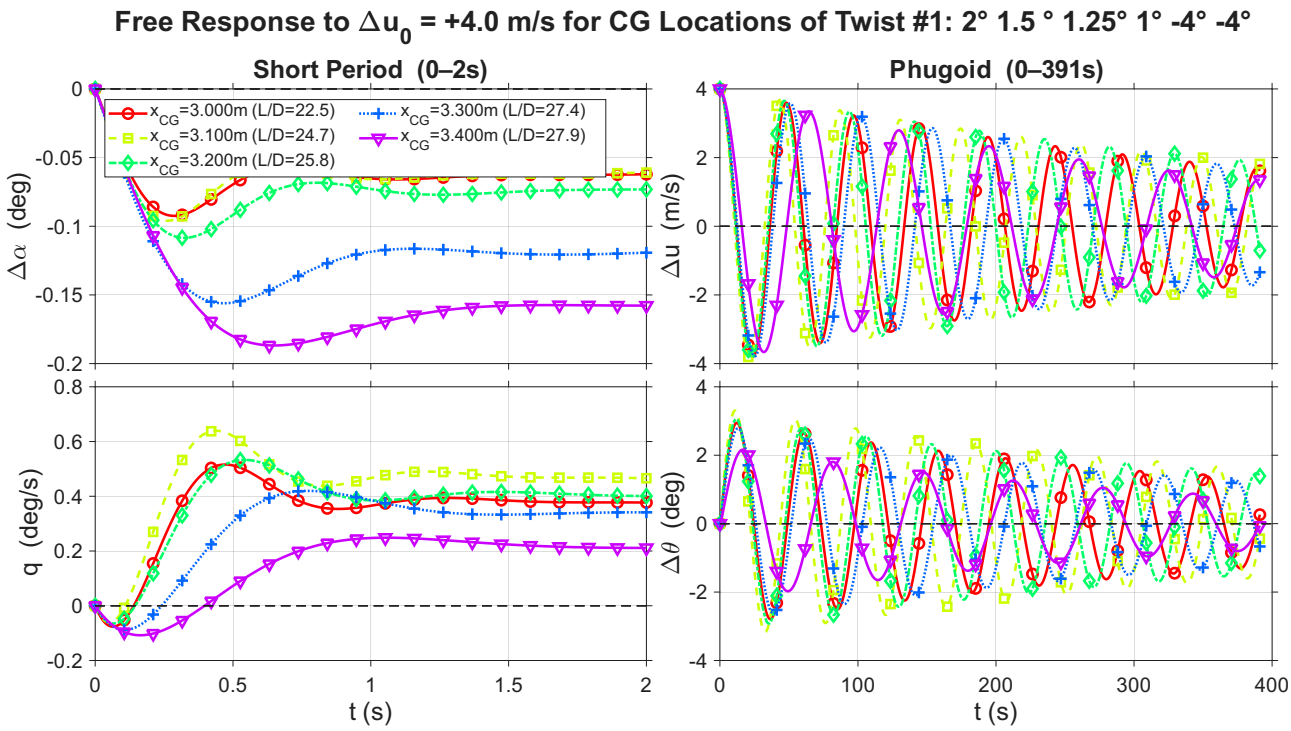


Figure 9 – Free response to an initial forward-velocity perturbation of $4\,\mathrm{m\,s^{-1}}$ for the twisted configuration number *1* and its stable CG positions showing the short-period (left) and phugoid (right) recovery.

As the center-of-gravity shifts rearward, the static margin decreases, and the lift-to-drag ratio increases from 22.5 to 27.9. The natural frequencies of both modes decrease, while their damping ratios increase. The short-period therefore becomes slower but more strongly damped towards the aft positions, whereas the most forward position exhibits the least short-period damping. The phugoid follows the same tendency.

All evaluated trim states for twist case *1* are summarized in Table 2, listing the angle-of-attack and elevon deflection at trim, the static margin, pitching-moment gradient, and the natural frequencies and damping ratios of both modes.

Table 2 – Characteristic parameters of case *1* showing the angle-of-attack and elevon deflection in trim state, pitching moment coefficient gradient, natural frequencies and damping ratios of the phugoid and short-period modes for all stable CG positions.

x_{CG}	α_{trim}	$\delta_{e,trim}$	SM	c_{m_α}	L/D	**Phugoid**		**Short-Period**	
(m)	(°)	(°)	(-)	(rad^{-1})	(-)	ω_n ($\mathrm{rad\,s}^{-1}$)	ζ (-)	ω_n ($\mathrm{rad\,s}^{-1}$)	ζ (-)
3.00	1.5	−8.26	0.1165	−0.4780	21.5	0.1206	0.0179	8.4943	0.3797
3.00	2.0	−9.31	0.1129	−0.4601	22.5	0.1291	0.0172	8.3502	0.3847
3.10	1.0	−6.20	0.0863	−0.3535	21.5	0.1096	0.0194	7.4151	0.4074
3.10	1.5	−7.06	0.0878	−0.3603	23.0	0.1202	0.0192	7.4785	0.4053
3.10	2.0	−7.92	0.0999	−0.4185	24.1	0.1320	0.0153	8.0037	0.3906
3.10	2.5	−8.80	0.1188	−0.5080	24.7	0.1439	0.0136	8.7448	0.3725
3.20	1.0	−5.05	0.0565	−0.2294	23.0	0.1052	0.0204	6.1441	0.4572
3.20	1.5	−5.72	0.0641	−0.2636	24.7	0.1189	0.0187	6.5214	0.4393
3.20	2.0	−6.38	0.0797	−0.3356	25.8	0.1334	0.0145	7.2519	0.4109
3.30	1.0	−3.76	0.0312	−0.1252	24.7	0.0915	0.0235	4.8187	0.5461
3.30	1.5	−4.19	0.0270	−0.1058	26.3	0.0955	0.0247	4.5170	0.5722
3.30	2.0	−4.63	0.0407	−0.1695	27.4	0.1221	0.0179	5.4323	0.4998
3.40	1.0	−2.29	0.0154	−0.0625	26.3	0.0603	0.0469	3.8131	0.6658
3.40	1.5	−2.46	0.0227	−0.0939	27.9	0.0964	0.0287	4.3602	0.5962

The data confirm a clear trend across the CG sweep. As the center-of-gravity shifts from $3.0\,\mathrm{m}$ to $3.4\,\mathrm{m}$, the static margin reduces from a maximum of approximately $11.9\,\%$ to a minimum of $1.5\,\%$ across the simulated operating points, comparable to values reported in the literature [35, 36]. The required trim elevon deflection decreases from about $-9°$ to $-2°$, confirming the reduced trim drag of the aft positions, yielding a higher L/D. For a fixed center-of-gravity position, increasing L/D ratios at the trim points results in lower phugoid damping, in agreement with the classical phugoid damping formulation, which scales inversely with the lift-to-drag ratio [14]. The natural frequencies, in turn, increase with the static margin and c_{m_α}.

From a handling-qualities perspective, the aft positions combine the highest aerodynamic efficiency and the most strongly damped short-period response with a very low static margin. The forward positions, in contrast, provide robust static stability with a high pitching moment gradient and static margin, but require larger elevon deflections, reduce the available control authority, and exhibit a more lightly damped, higher-frequency short-period and phugoid response. The narrow admissible center-of-gravity range and the low static margins indicate that an active flight-control augmentation system may be required to ensure satisfactory handling qualities across the operating envelope, which remains to be analyzed.

3.5 Prediction of Aerodynamic Coefficients by the Panel-Method and Computational Fluid Dynamics

Initial studies have been conducted with OpenVSP and its underlying panel solver within VSPAERO. These potential-flow methods do not capture viscous effects, and the geometric discretization through quadrilateral panels is generally coarser than the volumetric meshes used in computational fluid dynamics. A discrepancy between the panel-method and Navier-Stokes-based solvers is therefore expected. To quantify these differences and assess the viability of the panel-method results, both methods are compared in terms of the lift and drag coefficients of the baseline geometry.

The CFD simulation is conducted in ANSYS CFX [37] using the Reynolds-Averaged Navier-Stokes (RANS) equations with the k-ω SST turbulence model, varying the angle-of-attack between $-14°$ and $24°$. Identical boundary conditions and reference states are applied for both methods. The resulting lift and drag coefficients are shown in Figure 10, with the CFD result plotted in blue and the VSPAERO panel-method result in red. A consistent discrepancy in the lift-curve slope c_{L_α} is observed.

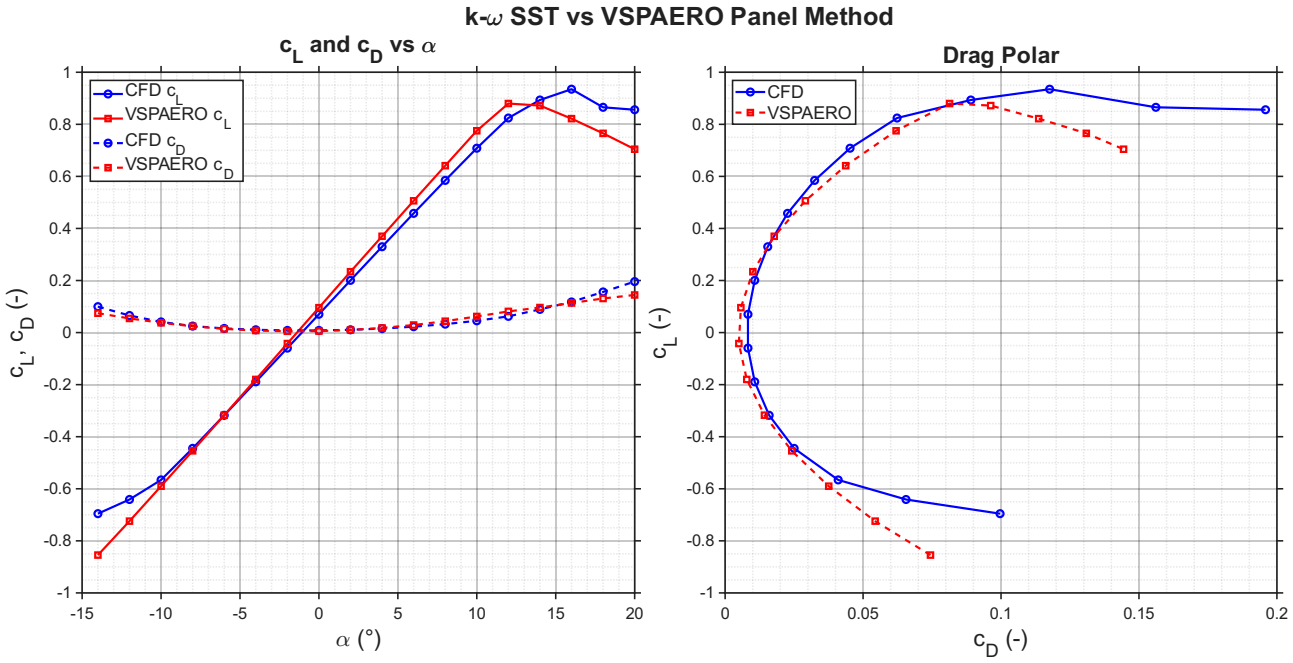


Figure 10 – Comparison of the panel-method and CFD predictions of the baseline configuration in terms of lift and drag coefficients over the angle-of-attack range.

The panel-method predicts a steeper slope than the CFD reference, which is expected for the potential flow formulation with its underlying inviscid flow assumption. The boundary-layer displacement thickness resolved by the CFD model is assumed to effectively modify the aerodynamic camber of the wing sections, which is expected to lower lift predictions, as reported by Lian and Shyy [38] in their work analyzing the effective airfoil shape under different turbulence levels.

The drag prediction in VSPAERO combines the induced drag c_{D_i} obtained directly from the potential-flow solution and an empirical parasite-drag estimate c_{D_0} that accounts for form-drag effects through wetted-area methods, based on the skin-friction formulation of Schlichting [39]. Viscous effects thus enter the drag prediction only through an analytical correction, without affecting the lift or moment distributions. The CFD result resolves the viscous boundary layer directly and couples skin-friction, pressure-drag, and lift contributions through its governing equations, which leads to a higher predicted total drag across the operating range. However, especially drag estimates obtained from RANS solvers must be interpreted with care, as the predicted values can vary between turbulence models and time-schemes, particularly in regions of incipient flow separation [40].

For the static and dynamic stability analysis presented in this work, the relevant operating range

lies within $\alpha \in [0°, 4°]$, where both methods predict linear aerodynamic behavior. Within this range, the panel-solver is considered applicable and is selected as the preferred method for the preliminary design analysis due to its substantially lower computational effort compared with CFD and its integration into the MATLAB-controlled parametric workflow within OpenVSP.

3.6 Current Design Stage

Based on the results of the wing-twist study and further evaluations not detailed herein, the aircraft design was iterated in the first step. The latest model, shown in Figure 11, considers the integration of the hydrogen tanks and propulsion units according to approximate size estimates based on current technological trends.

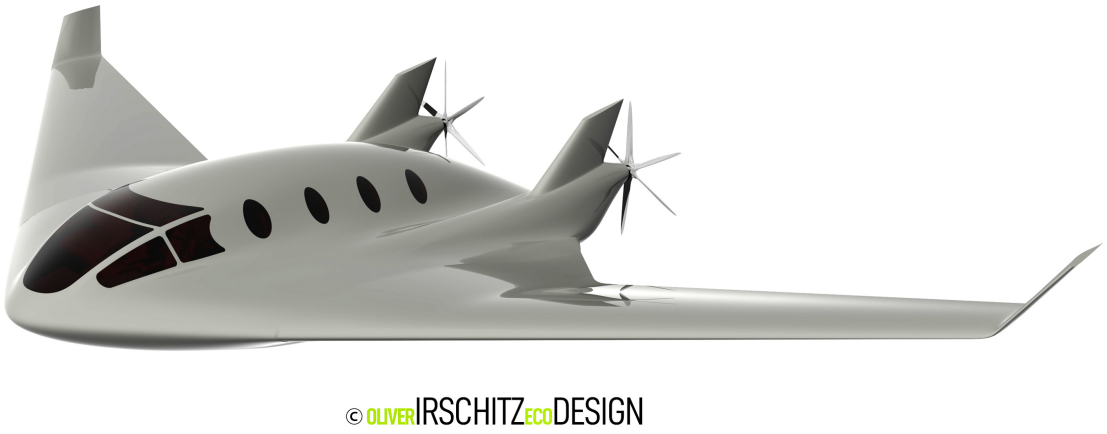


Figure 11 – Current design iteration of the fuel-cell powered flying wing.

Their integration required considerable changes to the configuration at the aircraft's cabin-root interface, while the wing-twist distribution identified in the previous study was retained. To address the lateral-directional dynamics, the aircraft employs drag fins to counteract yawing moments; their effectiveness remains to be studied.

Since the admissible center-of-gravity travel remains limited at this stage, an increased leading-edge sweep is being investigated to shift the neutral point further rearward while additionally extending the moment arm of the elevons. A larger moment arm reduces the elevon deflection required for trim and thereby lowers the trim drag, widening the range of attainable trim states. However, at constant wing area, an increased sweep reduces the effective wingspan and therefore the aspect ratio, which strengthens the wingtip vortices and increases the induced drag. The resulting trade-off between extended CG travel and aerodynamic efficiency will be assessed in future design iterations.

4. Conclusion and Outlook

This paper presents a systematic longitudinal aerodynamic pre-design methodology for a fuel-cell-powered flying wing targeting CS-23 certification as the first step in a broader multi-fidelity design workflow. Wing twist, center-of-gravity location, elevon trim deflection at a given angle-of-attack, and longitudinal dynamic stability were coupled within a parametric study conducted with the OpenVSP panel-method, controlled through MATLAB. Grid convergence of the panel-model was established via Richardson extrapolation.

A comprehensive wing-twist study showed that a spanload distribution, compared to the theoretically ideal bell lift distribution, can improve roll-turn behavior, thereby enhancing the aircraft's flying properties. The untwisted baseline produced only three feasible trim points throughout a CG analysis, whereas the twisted candidates yielded approximately fifteen, expanding CG travel from $0.1\,\mathrm{m}$ to $0.4\,\mathrm{m}$. Wing twist is therefore a primary design driver, with a modest efficiency penalty relative to an elliptical lift distribution. Across the CG sweep from $x_{\mathrm{CG}} = 3.0\,\mathrm{m}$ to $3.4\,\mathrm{m}$, the static margin decreased from a maximum of $11.9\,\%$ to a minimum of $1.5\,\%$, while the short-period natural frequency decreased

from $8.5\,\mathrm{rad\,s^{-1}}$ to $3.8\,\mathrm{rad\,s^{-1}}$, considering all feasible trim points. The short-period damping ratio increased from 0.38 to 0.70 for a twisted wing. The phugoid remained dynamically stable throughout and showed no modal instability in the analyzed linear model; however, formal compliance with the qualitative CS-23 handling-quality requirements necessitates further assessment. The comparison with a higher-fidelity CFD simulation supports the use of the panel method as an appropriate tool within the stability-relevant angle-of-attack range $\alpha \in [0°, 4°]$, although the moment coefficients and stability derivatives have not yet been validated.

The current design iteration incorporates hydrogen-tank and propulsion dummy volumes, requiring reassessment of the aerodynamic characteristics at the updated cabin-root interface. Lateral-directional stability analysis, including evaluation of the drag-fin effectiveness and characterization of the Dutch roll and spiral modes, represents the next step, with the bell-spanload twist distribution providing a favorable starting point. Thermal management of the fuel-cell and environmental control system will require additional internal aerodynamic analyzes of the ducting and venting architecture needed to optimize cooling performance against cooling drag penalties. The next step includes the assessment of increased leading-edge sweep for extended CG travel and static margin, propulsion-airframe interaction, and the finalization of mass and CG locations across the CG/weight envelope since the current model does not assume weight distribution in detail.

5. Acknowledgement

This work was supported by the Austrian Federal Ministry for Climate Action, Environment, Energy, Mobility, Innovation, and Technology (BMK) under the program Take-Off via the project FlySIC (FO999927732).

6. Contact Author Email Address

philip.kirschnek@fh-joanneum.at

7. Copyright Statement

The authors confirm that they, and/or their company or organization, hold copyright on all of the original material included in this paper. The authors also confirm that they have obtained permission, from the copyright holder of any third party material included in this paper, to publish it as part of their paper. The authors confirm that they give permission, or have obtained permission from the copyright holder of this paper, for the publication and distribution of this paper as part of the ICAS proceedings or as individual off-prints from the proceedings.

References

[1] Müller F. *Flugzeugentwurf: Entwurfssystematik, Aerodynamik, Flugmechanik und Auslegungsparameter für kleinere Flugzeuge*. D. Thomas, 2003.

[2] Abrantes I, Ferreira A F, Magalhães L B, Costa M, and Silva A. The impact of revolutionary aircraft designs on global aviation emissions. *Renewable Energy*, 223:119937, 2024.

[3] Martins J R R A. Aerodynamic design optimization: Challenges and perspectives. *Computers Fluids*, 239:105391, 2022.

[4] Bravo-Mosquera P D, Catalano F M, and Zingg D W. Unconventional aircraft for civil aviation: A review of concepts and design methodologies. *Progress in Aerospace Sciences*, 131:100813, 2022.

[5] Zountouridou E, Kiokes G, Dimeas A, and Prousalidis J. A guide to unmanned aerial vehicles performance analysis—the mq-9 unmanned air vehicle case study. *The Journal of Engineering*, 2023.

[6] Prandtl L. Über Tragflügel Kleinsten Induzierten Widerstandes. In *Zeitschrift für Flugtechnik und Motorluftschiffahrt*, 1933.

[7] Bowers A H, Murillo O J, Jensen R R, Eslinger B, and Gelzer C. On wings of the minimum induced drag: Spanload implications for aircraft and birds. Technical report, 2016.

[8] Faggiano F, Vos R, Baan M, and Van Dijk R. Aerodynamic Design of a Flying V Aircraft. In *17th AIAA Aviation Technology, Integration, and Operations Conference*, Denver, Colorado, 2017.

[9] Liebeck R H. Design of the Blended Wing Body Subsonic Transport. *Journal of Aircraft*, 2004.

[10] Prandtl L. Applications of modern hydrodynamics to aeronautics. *NACA Report No. 116*, 1923.

[11] Houghton E L, Carpenter P W, Collicott S H, and Valentine D T. Chapter 5 – Wing Theory. In *Aerodynamics for Engineering Students (Sixth Edition)*, pages 269–347. Butterworth-Heinemann, Boston, 6th edition, 2013.

[12] European Aviation Safety Agency. CS-23: Certification Specifications for Normal, Utility, Aerobatic, and Commuter Aeroplanes - Amendment 3, July 2012.

[13] Etkin B and Reid L D. *Dynamics of Flight: Stability and Control*. John Wiley & Sons, 1995.

[14] Nelson R C. *Flight Stability and Automatic Control*, volume 2. WCB/McGraw Hill New York, 1998.

[15] Abbott I H and Von Doenhoff A E. *Theory of Wing Sections: Including a Summary of Airfoil Data*. Courier Corporation, 1959.

[16] Anderson J D Jr. *Fundamentals of Aerodynamics*. McGraw-Hill Education, 5th ed. edition, 2011.

[17] Nickel K, Wohlfahrt M, and Brown E M. *Tailless aircraft in theory and practice*. AIAA Education, 1994.

[18] Mader C and Martins J R R A. Stability-Constrained Aerodynamic Shape Optimization of a Flying Wing Configuration. In *13th AIAA/ISSMO Multidisciplinary Analysis Optimization Conference*, 2010.

[19] Murman S M. Reduced-Frequency Approach for Calculating Dynamic Derivatives. *AIAA Journal*, 45(6):1161–1168, 2007.

[20] Etkin B. *Dynamics of Atmospheric Flight*. Courier Corporation, 2005.

[21] Da Ronch A, McCracken A J, Badcock K J, Widhalm M, and Campobasso M S. Linear frequency domain and harmonic balance predictions of dynamic derivatives. *Journal of Aircraft*, 50(3):694–707, 2013.

[22] Katz J and Plotkin A. *Low-Speed Aerodynamics*. Cambridge University Press, 2001.

[23] The MathWorks Inc. Matlab version: R2025b, 2025.

[24] National Aeronautics and Space Administration. Open vehicle sketch pad, 2025.

[25] Maskew B. Program VSAERO Theory Document: A Computer Program for Calculating Nonlinear Aerodynamic Characteristics of Arbitrary Configurations. Technical report, NASA, 1987.

[26] Kaushik M. *Theoretical and Experimental Aerodynamics*. Springer Nature Singapore, 2019.

[27] Erickson L L. Panel Methods – An Introduction. Technical Report NASA-TP-2995, NASA Ames Research Center, Moffett Field, CA, 1990.

[28] Morino L and Kuo C C. Subsonic Potential Aerodynamics for Complex Configurations: A General Theory. *AIAA Journal*, 12(2):191–197, 1974.

[29] Stevens B L, Lewis F L, and Johnson E N. *Aircraft Control and Simulation: Dynamics, Controls Design, and Autonomous Systems*. John Wiley & Sons, Hoboken, NJ, 3rd edition, 2015.

[30] Roache P J. Quantification of Uncertainty in Computational Fluid Dynamics. *Annual Review of Fluid Mechanics*, 29(1):123–160, 1997.

[31] Celik I B, Ghia U, Roache P J, Freitas C J, Coleman H, and Raad P E L. Procedure for Estimation and Reporting of Uncertainty Due to Discretization in CFD Applications. 130(7), 2008.

[32] Engels H. Zur Anwendung der Richardson-Extrapolation auf die numerische Differentiation. *Computing*, 8(3):255–271, 1971.

[33] Torenbeek E. Aerodynamic Performance of Wing-Body Configurations and the Flying Wing. Technical report, SAE Technical Paper, 1991.

[34] Liebeck R H, Page M A, and Rawdon B K. Evolution of the Revolutionary Blended-Wing-Body. *Transportation Beyond 2000: Technologies Needed for Engineering Design*, 1996.

[35] Tran D T, Pham V K, Nguyen A T, and Nguyen D T. Aerodynamic Design Optimization for Flying Wing Gliders Based on the Combination of Artificial Neural Networks and Genetic Algorithms. *Aerospace*, 12(9), 2025.

[36] Cook M V and de Castro H V. The longitudinal flying qualities of a blended-wing-body civil transport aircraft. *The Aeronautical Journal*, 108(1080):75–84, 2004.

[37] ANSYS, Inc. ANSYS CFX, Release 2024 R2. ANSYS, Inc. Software, 2025.

[38] Lian Y and Shyy W. Laminar-Turbulent Transition of a Low Reynolds Number Rigid or Flexible Airfoil. *AIAA Journal*, 45:1501–1513, 07 2007.

[39] Schlichting H and Gersten K. *Boundary-Layer Theory*. Springer, 2016.

[40] Gan J, Shen Y, and Zha G. Comparison of Drag Prediction Using RANS models and DDES for the DLR-F6 Configuration Using High Order Schemes. In *54th AIAA Aerospace Sciences Meeting*, 2016.